

Lawrence Berkeley National Laboratory

Lawrence Berkeley National Laboratory

Title

On-Site Geologic Core Analysis Using a Portable X-ray Computed Tomographic System

Permalink

<https://escholarship.org/uc/item/6xj835nh>

Authors

Freifeld, Barry M.
Kneafsey, Timothy J.
Rack, Frank

Publication Date

2004-03-01

Peer reviewed

On-site Geologic Core Analysis Using a Portable X-ray Computed Tomographic System

By Barry M. Freifeld¹, Timothy J. Kneafsey¹, and Frank Rack²

¹ Lawrence Berkeley National Laboratory, Berkeley, CA, USA

² Joint Oceanographic Institutions, Washington DC, USA

X-ray computed tomography (CT) is an established technique for nondestructively characterizing geologic cores. CT provides information on sediment structure, diagenetic alteration, fractures, flow channels and barriers, porosity, and fluid-phase saturation. A portable CT imaging system has been developed specifically for imaging whole-round cores at the drilling site. The new system relies upon carefully designed radiological shielding to minimize the size and weight of the resulting instrument. Specialized x-ray beam collimators and filters maximize system sensitivity and performance. The system has been successfully deployed on the research vessel *Joides Resolution* for Ocean Drilling Program's Leg 204 and 210, within the Ocean Drilling Program's refrigerated Gulf Coast Core Repository, as well as on the Hot Ice #1 drilling platform located near the Kuparuk Field, Alaska. A methodology for performing simple densitometry measurements, as well as scanning for gross structural features, will be presented using radiographs from ODP Leg 204. Reconstructed CT images from Hot Ice #1 will demonstrate the use of CT for discerning core textural features. To demonstrate the use of CT to quantitatively interpret dynamic processes, we calculate 95% confidence intervals for density changes occurring during a laboratory methane hydrate dissociation experiment. The field deployment of a CT represents a paradigm shift in core characterization, opening up the possibility for rapid systematic characterization of three-dimensional structural features and leading to improved subsampling and core-processing procedures.

Introduction

Radiographic imaging has been used since 1947 [Boyer et al.] to determine oil saturation in cores and to investigate fluid flow [Morgan et al., 1950]. The development of x-ray computed tomography (CT) by Hounsfield [1972] sparked a revolution in x-ray imaging by enabling the nondestructive estimation of density with high spatial resolution, based on the reconstruction of a series of radiographs. Currently, x-ray CT is used to nondestructively characterize geologic samples and investigate dynamic processes. Computed tomographic images reveal sediment structure, diagenetic alterations, fractures and flow paths, – and permit a large range of other properties to be inferred from quantitative densitometry. CT also allows the intelligent selection of appropriate subsampling locations by revealing the internal structure of a whole core.

Early pioneering x-ray CT work for soil science applications was performed by Petrovic et al. [1982] looking at bulk soil density, and Hainsworth and Aylmore [1986], studying water saturation distribution. In the petroleum engineering field, Vinegar [1986] and Wellington and Vinegar [1987] laid a comprehensive foundation for performing

petrophysical characterization of oil-bearing units, enhanced oil recovery experiments and multiphase relative permeability measurements using x-ray CT. To date, most of the work performed on geologic core characterization has been performed using medical scanners, which are designed for imaging the human body and not optimized for core characterization.

The portable CT system described herein has been designed specifically for core characterization. Unlike medical systems that require the user to exit the room during system operation, a novel radiological shielding arrangement minimizes the weight and volume of the system and permits operation of the x-ray in close quarters. To produce the highest-quality three-dimensional images, we have designed an x-ray compensator, similar in purpose to the compensators used in early medical systems, that reduces image saturation beyond the edge of the core and improves system sensitivity.

The new system has been used on the *JOIDES Resolution* during the Ocean Drilling Program's (ODP) Leg 204 and Leg 210 to image whole-round cores, as well as within the ODP's refrigerated Gulf Coast Core Repository. The system was also used at Hot Ice #1, a methane hydrate research drilling project on the North Slope of Alaska. At the Hot Ice #1 drill site, the system was operated in a room at subfreezing temperatures to stabilize permafrost cores and reduce the rate at which any recovered hydrate would decompose. This paper details the portable x-ray CT system design, shows examples of acquired data, and uses a methane hydrate dissociation experiment to demonstrate the system's quantitative capabilities. Suggestions on future research activities, and areas needing attention for improving x-ray CT core analysis, are presented in the paper's conclusions.

System Description

A schematic layout and photograph of the portable CT installed on the Bridge Deck of the *JOIDES Resolution* are shown in Figure 1. The core is installed vertically in the instrument and rotated around its vertical axis. A horizontal gantry holding the x-ray source and detector is raised and lowered by a belt-driven actuator to facilitate imaging selected regions of the core. The x-ray source has a tungsten target and a 250 μm thick beryllium window, delivering up to 130 kV at 0.5 mA, with a variable focal spot size that increases from 5 microns at 4 watts to 100 microns at 65 watts. Computer control permits adjustment of both anode voltage and current. To be able to efficiently capture the cone-beam projection of the core, we used a dual-field 100 mm/150 mm cesium iodide image intensifier. The image intensifier exhibits some geometrical distortion (commonly referred to as pin-cushioning) and lacks the dynamic range of available solid-state x-ray detectors, but rapidly acquires images and has high sensitivity. Rapid imaging is important for imaging large numbers of cores and for performing transient studies.

Resolution of the CT system is dependent on numerous system parameters, including x-ray source focal spot size, image intensifier phosphor properties, location of the core between the x-ray source and the image intensifier, CCD camera resolution, and the image intensifier field of view. For the CT images shown in this paper, x-ray spot size varied from 60 to 100 μm depending on power setting, the image intensifier input

window was kept fixed at 150 mm in diameter, and the camera resolution was 768×494 . With these settings, pixels on the acquired radiographs were approximately $200 \mu\text{m}^2$, resulting in reconstructed voxels ($200 \mu\text{m}$ on a side) that have a volume of 8 nanoliters.

To reduce noise and increase the dynamic range of the system, great care was taken to optimize the x-ray beam path for core imaging. A beam collimator mounted on the x-ray source was used to minimize albedo, which degrades image quality. To reduce camera noise, multiple frames are acquired and averaged without moving the object, leading to a noise reduction proportional to the square root of the number of frames. Ten frames acquired over a 0.4-second period was considered a reasonable trade-off between speed and image quality for the images acquired in this paper, although that number can be adjusted to match the requirements of the user's particular application.

As part of the beam collimator, a computer-controlled copper shutter mounted in front of the beryllium exit window can optionally be used to reduce the soft x-ray content of the beam. This is normally only performed at energies above 100 kV to reduce the influence that the effective atomic number has on x-ray attenuation, and lead to more precise density estimates. Below 100 kV, there is a significant component of photoelectric absorption, which is proportional to effective atomic number. Reducing the x-ray voltage (softer x-rays) results in increased photoelectric absorption and serves to highlight contrasting media and differences in fluid-phase saturation. This also leads to greater uncertainty in the density estimates because of increased beam-hardening effects (filtering of soft x-rays). A concise discussion of the effects of spectral energy, including implications for core analysis, is provided by Wellington and Vinegar [1987].

An aluminum compensator (Figure 2), installed between the sample and x-ray imager, reduces the dynamic range of the x-rays incident upon the image intensifier and increases sensitivity to attenuation variations within the sample. Because of the geometry of passing a cone-shaped beam through a cylindrical object, the x-rays passing beyond the outside edge of the coreholder are not attenuated by the object; thus, the compensator is thickest in this region. By greatly attenuating the x-ray beyond the edge of the core holder, the aluminum compensator eliminates image blooming, an image defect that involves pixels on a CCD approaching their electron charge capacity and spilling over into nearby pixels, washing out the image. Where the core is thickest, in the center, the attenuator is thin, providing minimal additional attenuation of the x-rays. The result is an image of fairly uniform intensity striking the image intensifier. The aspherical compensator is designed using a fan-beam x-ray path simulation, assuming a core of uniform density. The slight variation in attenuation that occurs along the vertical axis of the core (as x-ray cone-beam angle increases) is ignored.

While the qualitative benefits of using the compensator have been mentioned above, Figure 3 provides a quantitative example of how density resolution can be improved by using the compensator, without having to resort to cameras with increased dynamic range. For this discussion, it should be mentioned that every radiograph is composed of pixels with an intensity spanning a range that can be digitally represented, i.e., 10 or 12 bits. Similarly, a dynamic range, or bit depth, can be assigned for any region of interest.

The dynamic range of a region of interest will be less than or equal to that of the whole image. As noted previously, without the compensator in place, a large variation in intensity occurs, from the outside of the core image to the inside. With the compensator in place, the dynamic range across the image is reduced, and greater contrast can be seen in any particular region of interest.

Figure 3 shows radiographic images of sandstone cores taken with the x-ray energy set below the threshold at which significant image blooming occurs, along with a histogram of pixel intensity for the region of interest enclosed in the white rectangles. The image taken without using the compensator was taken with the x-ray source set to 90 kV and 250 μ A, whereas the image with the compensator was taken at 110 kV and 300 μ A. For the region of interest without the compensator, the histogram reveals an image bit depth of 6 bits. The image with the compensator has a bit depth of 7.7 bits, representing a more than three fold increase in the x-ray attenuation resolution. The increased performance provided by the compensator is significant.

The aluminum compensator also contains milled flats that extend beyond the edges of the acylindrical region, used for correcting for fluctuations in x-ray tube intensity. By normalizing each image by the average image intensity in the reference region, one source of errors in density estimates is eliminated. This is particularly important for experiments that span long time periods, such as petroleum core floods, which can span several weeks duration. Note that large variations in x-ray current can be corrected for using this method, but because of photoelectric absorption, changes in x-ray voltage beyond small ripples produce nonlinear changes in the image intensity. Thus x-ray tube current can vary over a broad range and all of the images can be normalized to each other. Any change in the voltage setting, however, will require an independent system calibration for each selected voltage.

The image reconstruction software, *Imgrec* (developed at Lawrence Livermore National Laboratory), was employed to perform fan-beam convolution back projection (CBP) and Feldkamp reconstruction of the acquired cone-beam radiographs [Feldkamp et al., 1984]. The CBP algorithm is used for rapid reconstruction of acquired radiographs to verify correct parameter settings (only a few seconds are required to reconstruct a single horizontal slice), but does not account for the divergent cone-beam projection geometry. This limits CBP to the region near the radiograph's mid-plane. The Feldkamp algorithm corrects for the divergent cone beam geometry and can be used to accurately reconstruct images with x-ray projection angles up to 6 or 7 degrees. However, beyond that point, the approximations that make the Feldkamp algorithm computationally tractable result in noticeable geometric distortions. The images shown in this paper have used cone-beam angles from 6 degrees to 10 degrees. The reconstruction of 180 radiographs into a 10 cm three-dimension volume data set takes approximately 10 minutes on a 3 GHz PC. For either the CBP or the Feldkamp algorithm, it is important to acquire both a dark image from the camera (an image with the x-ray beam off) and a background image (where no object is in the beam path), which is subtracted from subsequent images of the object to account for x-ray intensity variations across the imaging plane.

Several innovations in the CT system make it both portable and radiologically safe for use in a core laboratory. The key to transportability is minimizing the volume enclosed within lead shielding. The usual shielding method for a fixed system, encapsulation of the entire unit or room within a lead enclosure, would have resulted in a unit of limited portability. We minimized the shielding required to enclose the x-ray path, by forming a cross that translates along the core axis (Figure 1). One arm of the cross encompassed the main x-ray beam, and the other arm reduces radiation scattered along the core axis. To permit loading and unloading of the core, we split the vertical arm of the cross, allowing it to open and close by telescoping back over the horizontal arm. The entire system is designed to meet the United States radiological requirements for a cabinet safe system (U.S. Title 21 Code of Federal Regulations §1020.40). Redundant safety interlocks are located both on the access door and the shielding, to prevent energizing the x-ray unit while personnel are manipulating the core.

To convert x-ray attenuation to density, we scan the reference materials and perform a three-dimensional CT reconstruction. A slice from a CT reconstruction of a calibration standard containing a variety of materials is shown in Figure 4. This standard consists of a 7.62 cm diameter PVC cylinder with a series of vertical holes, each of which contains a rod of different materials. For this standard, Figure 5 shows density versus attenuation, along with regression analysis of the data. The data for PVC is not used for creating the calibration curve, because the high atomic number of the chlorine contributes to a significant photoelectric absorption component in the x-ray attenuation, resulting in an overestimated density.

The CT reconstructed image of the calibration cylinder displays artifacts and aberrations that are worth noting. Geometrically, because of image intensifier pin-cushioning, there is some visible elongation of the reference rods, which should appear circular. This aberration can be removed by remapping the pixels on each radiograph to eliminate the distortion prior to performing CT reconstruction. Quantitatively, there are negligible changes in the estimated material densities due to geometrical distortion. Beam-hardening, due to the polychromatic nature of the x-ray beam, is a reconstruction artifact responsible for the PVC cylinder appearing brighter in the center than at the edges. Unlike typical beam-hardening that make the outer edges of an object appear more dense (since it attenuates soft x-rays) and the center appear less dense (due to the interaction with harder x-rays), the aluminum compensator adds a counterintuitive beam-hardening aberration. This is because the background correction image used to normalize for intensity variation across the image intensifier suffers from beam-hardening effects, making the image appear disproportionately dark at the edges and bright at the center. The background corrected CT core images thus appear bright (less dense) at the edges, and dark (more dense) in the center.

There are several ways to eliminate or correct for beam-hardening effects when using the compensator. The simplest method is to perform a polynomial correction to the radiographs that removes the beam-hardening trend. This is the method that has been applied to the images in this paper. The second method, which will be carried out in the future, is to design the compensator using a polychromatic ray-path simulation.

Deployment on Ocean Drilling Program Leg 204

The portable x-ray CT system was first deployed on the *Joides Resolution* for Ocean Drilling Program Leg 204, Drilling for Hydrates at Hydrate Ridge, Cascadia Continental Margin, approximately 50 nautical miles from the Oregon Coast. A radiation safety check was performed to verify that no hidden damage occurred to the radiation shielding during transport, and training of *Joides Resolution* technical staff was conducted. Both the portability and ease of use of the CT system were demonstrated by the CT system's set-up and operation within a 12-hour period.

During Leg 204, the CT system was used in two different modes: (1) to linearly scan the core, taking two images at 90 degree orientation to each other at 10 cm intervals along the length of the core and (2) in CT mode, which acquires 180 images with a two degree core rotation between each image. In less than two minutes, the linear imaging mode captures gross structural features along the entire length of a 1.5 m core. This data can be used to perform high resolution densitometry. Over 12,000 radiographs from more than 500 cores were acquired during Leg 204, with the images available for both real-time viewing and electronic archival storage. The CT imaging mode takes between one and three minutes to image a 10 cm core section, depending on the final desired resolution.

The radiographic images provide quantitative densitometric measurements with high spatial resolution. An alternative measurement technique for performing systematic density measurements from whole cores, which is part of the *Joides Resolution*'s multi-sensor core logging system [Blum, 1996], is Cs¹³⁷ gamma ray densitometer (GRD). The GRD provides an integrated average density along the mid-line of the core over a 1 cm² area, with a typical sample frequency of one data point every 2.5 cm. The spacing of GRD data points is limited because it takes several seconds (e.g. 4 seconds for a 7 cm diameter core) to acquire each measurement. The x-ray radiographs provide a two dimensional data set with a resolution of 200 μm. By acquiring two images at 90 degree orientation to each other, the x-ray provides some indication as to gross structural inhomogeneities that may be ambiguous from a single image.

The radiographs taken during linear scanning reveal more than just gross structural features and densitometric data. Small heterogeneities with enough density contrast are apparent, particularly if the supporting matrix is fairly uniform. As an example, a radiograph taken from ODP Leg 204 Site 1251B15 showing dark sulfide deposits filling in former bioturbation features is shown in Figure 6. The bright horizontal fractures are created by gas evolution during core recovery, which results in significant changes in the core fabric.

To estimate density using the x-ray radiographs, three processing steps are performed. The first step is to correct for fluctuations in the energy emitted from the x-ray source using the reference region from the aluminum compensator. Second, geometrical effects (scanning through the cylindrical core and compensator using a divergent cone-beam) are corrected by normalizing each acquired radiograph by an ideal image generated by a

homogeneous core. This image can either be calculated theoretically or obtained experimentally. For this paper, an experimentally obtained image from a homogeneous sediment core was used to normalize the radiographs. Finally, the normalized data is converted from corrected attenuation to density, using a linear calibration like the one shown in Figure 5.

Figure 7 shows radiography data from ODP Leg 204, Site 1251B37 compared to GRD, gravimetric-based moisture and density measurements, along with logging-while-drilling (LWD) density logs taken in nearby ODP Leg 204 1251A [Tréhu et al, 2003]. Density estimates using the x-ray radiography, GRD, and LWD data are plotted every 2 mm, 2.5 cm and every 15 cm, respectively. The x-ray radiography density estimate is calculated using the average attenuation measured for the 100 pixels contained within a 2×2 mm region.

All three core based methods are able to identify a dense carbonate-rich feature a few centimeters in length at 305.45 mbsf. Only the x-ray radiographs are able to reveal the lateral extent of this feature across the core, as well as the presence of another thin dense feature at 305.32 mbsf. Since the LWD was not taken in the same borehole, a direct comparison for this particular feature is not possible. The radiographic data, (i.e., between 306.4 and 306.5 mbsf.) show very-well-defined areas of core disturbance interspersed between regions of intact core. Because of the limited spatial resolution of the GRD measurements, areas of the core that are heavily disturbed by gas exsolution appear as increased noise in the data. As expected, the LWD measurement displays none of the artifacts that arise from core recovery. It is encouraging that all of these methods offer very good overall agreement for both density trends and absolute estimated value.

Hot Ice #1 Methane Hydrate Research Well

Methane hydrate is a naturally occurring clathrate compound, commonly found within deep oceanic or permafrost regions. In methane hydrate, crystalline water encages a gas molecule. Interest in naturally occurring gas hydrates is increasing because of their energy resource potential, as well as their role in climate variability [Kvenvolden, 1988]. An exploratory hydrate drilling program, Hot Ice #1, targeting the Sagavanirktok Formation was drilled down to 427 m in April 2003, and completed February 2004 to a total depth of 701 m. The portable x-ray CT was operated as part of a mobile laboratory to nondestructively image cores recovered during both drilling operations. The room in which the x-ray CT was operated was kept at temperatures between -10°C and -5°C , to prevent deterioration of the permafrost cores and to minimize dissociation of any recovered hydrates. Dissociation of hydrate is the phase-change transformation from the crystalline hydrate to distinct water (either liquid or solid) and gas phases.

Prior to the initial mobilization to Hot Ice #1, hydrate dissociation studies were conducted, using the x-ray CT scanner, to spatially and temporally track the conversion of methane hydrate to methane and water ice using synthetic methane hydrate samples. Figure 8 shows a simplified schematic of the hydrate dissociation experiment. The synthetic hydrate was manufactured by the method detailed in Stern et al. [1996] and

combined with water ice and sand in a sealed pressure vessel. Hydrate dissociation, stimulated by allowing the room air to warm the sample in the pressure vessel, was monitored by measuring the temperature and pressure and periodically acquiring CT data [Freifeld and Kneafsey, 2003]. The goal was to determine how sensitive CT imaging is to spatial and temporal changes that occur during the hydrate dissociation process, so that these measurements can be applied to natural hydrate-bearing samples recovered during the Hot Ice #1 coring operation.

Figure 9 shows a sequence of reconstructed CT slices tracking the progression of dissociation of the synthetic methane hydrate. Differential images, created by subtracting the baseline image from subsequent images, are used to highlight relatively subtle changes in density as dissociation progresses. The difference in the images taken prior to the start of the dissociation process, and after dissociation is complete (as verified by the pressure in the vessel), yields estimates of total hydrate saturation and spatial distribution. Quantifying hydrate dissociation changes in the CT data depends on accurate system calibration, and high resolution densitometry. Since any one voxel has considerable noise, confidence in density estimates can be increased by averaging multiple voxels, assuming that the region averaged over is homogeneous, and any variation in measured attenuation results from normally distributed noise. The 95% confidence interval for an estimate can be expressed as

$$\rho_{0.95}(x) = \rho(x) \pm t_{0.95,n} \frac{\sigma}{\sqrt{n}}$$

where n is the number of voxels, σ is the standard deviation of density estimates, and t is Student's t distribution. Water ice is used as a reference material because its density will remain constant throughout this experiment. The 95% confidence interval for estimating the density change for the water ice is shown in Figure 10a as a function of the length of a cubical region of interest. As the cubic region of interest is increased to a few millimeters in length, the uncertainty declines to ± 0.01 g/cc.

Figure 10b shows the 95% confidence intervals for hydrate density changes during dissociation as a function of cubic region of interest, taken at three different times after the start of the experiment. As the hydrate dissociates and methane gas evolves, the density of the hydrate is seen to decrease. At the start of the experiment, the density of the methane gas engaged in the porous hydrate is calculated to be 0.084 g/cc, based on the stoichiometric ratio between water and methane. The density reduction as calculated from the x-ray images at 44 minutes, after dissociation concluded, is 0.088 g/cc. These density changes rely upon an initial baseline CT calibration curve, using regions of interest containing sand, hydrate and ice and their known densities. Figure 10b shows that even though x-ray CT system resolution may be 200 μm , if the objective is to determine small changes in hydrate saturation, then the smallest region of interest that yields reasonable confidence has a minimum spatial dimension of approximately a 2.5 mm cube, or roughly 2,000 voxels.

The sedimentary structure at Hot Ice #1 contains thick sequences of conglomerates, sandstones, mudstones, and coals. Coring operations recovered no hydrates, which was corroborated by standard geophysical logs and the general absence of finding significant gas bearing formations. X-ray CT images were acquired of more than 200 one-meter-long core tubes. Operationally, the only problem to note from work at the Arctic Platform Mobile Laboratory, in a space maintained at -5°C to -10°C , was the failure of a coating on one of the objective lenses in the image intensifier. The coating appeared to delaminate, causing a slight distortion in one portion of the image. This problem did not occur when the system was operated at the warmer, 2°C to 6°C temperatures within the Ocean Drilling Program's Gulf Coast Core Repository.

A CT image of permafrost sandstone recovered at Hot Ice #1 (210.7 mbgs.) is shown in Figure 11. The slice shown from the three dimension data set is a midcore vertical plane, resulting from averaging five $200\ \mu\text{m}$ thick slices. The core displays numerous interbedded laminae, ranging from wispy millimeter-sized fining layers, as shown in the upper detail, to organic interbeds containing small claystone clasts. The dark subhorizontal feature near the top of the core is an ice lens that has formed near a set of fine sand laminae. Changes in bedding strike and dip are clearly visible and can be used to define strike set thicknesses for various sedimentary layers.

Figure 12 shows vertical and horizontal CT images taken of three different core samples collected during Hot Ice #1. Figure 12(a) shows vertical CT images of an unlithified sand (570.3 mbgs) with interspersed, rounded mollusk-shell fragments. The dense (bright) region near the top of the core is an iron claystone concrete. Figure 12(b) shows horizontal CT images of a conglomerate cemented in a sand/ice matrix bearing numerous ice lenses. Individual gravel-sized fragments and small claystone clasts are visible. In Figure 12(c), horizontal CT images reveal abundant intact mussel fossils contrasting with the fine sand matrix.

Conclusions

X-ray CT imaging of recovered core adds significantly to the amount of information that can be systematically obtained in the field. Structural information, porosity, and phase-saturation can be obtained. High-resolution images of whole-core permit intelligent subsampling locations to be chosen so that they either intersect or avoid specific features. The portable system detailed here offers significant improvements in image quality over previous x-ray CT systems by incorporating specially designed collimators and filters to optimize the x-ray beam path.

By minimizing the sample volume enclosed by radiation shielding, carefully selecting ruggedized components, and by severely limiting infrastructure requirements, the x-ray CT we developed is able to be easily transported and operated. The vertical core orientation minimizes the footprint of the instrument, so that it can be easily incorporated into working lab space. By performing imaging at the drilling location, the highest quality data can be obtained before transport and storage lead to core degradation. This is

especially important when looking at ephemeral properties, such as gas hydrate saturation.

While the portable CT system shown here represents a paradigm shift from previous systems, numerous areas are open for continued development. These areas include incorporation of dual-energy techniques for mineral identification and improved density estimation, data mining software for identifying particular features or structures, and integration of the CT system into multiproperty measurement systems. The interface for accessing the enormous volume of data acquired in high-resolution three-dimensional imaging needs improvement, requiring advances in data handling and interpretation software.

Acknowledgments

This work was supported by the Assistant Secretary of the Office of Fossil Energy, Office of Natural Gas and Petroleum Technology, U.S. Department of Energy under Contract No. DE-AC03-76SF00098. The authors would also like to thank Dan Schneberk for making the CT image-processing code, *Imgrec*, available to us and Jacob Pruess for assistance in data analysis. In addition, we would like to thank Liviu Tomutsa for his careful review.

References

- Blum, P., Physical properties handbook: a guide to the shipboard measurement of physical properties of deep-sea cores. Chap. 3 Gamma-Ray Densimetry, (1997) *ODP Tech. Note*, 26 [Online]. Available from World Wide Web: <<http://www-odp.tamu.edu/publications/tnotes/tn26/INDEX.HTM>>.
- Boyer, R., Morgan, F., and Muskat, M., "A new method for measurement of oil saturation in cores," *Petroleum Transactions*, AIME, (1947) 170, 15–33.
- Feldkamp, L. A., Davis, L. C. and Kress, J. W. "Practical cone-beam algorithm," *J. Opt. Soc. Am. A* (1984) 1, 612–619.
- Freifeld, B. M. and Kneafsey, T. J., "Investigating methane hydrate in sediments using x-ray computed tomography," in *Advances in the Study of Gas Hydrates*, (2004) Kluwer Academic/Plenum Publishers, New York
- Hainsworth, J.M. and Aylmore, L.A.G., "The use of computer assisted tomography to determine the spatial distribution of soil water content," *Aust. J. Soil Res.* (1983) 21, 435–443.
- Hounsfield, G.N., "Computerized transverse axial scanning (tomography): Part I, Description of system," *British Journal of Radiology* (1973) 46, 1016–1022.

Kvenvolden, K. A. "Methane hydrate – a major reservoir of carbon in the shallow geosphere," *Chem. Geol.* (1988) **71**, 41-51

Morgan, F., McDowell, J., and Doty, E., "Improvements in the x-ray saturation technique of studying fluid flow," *Petroleum Transactions*, AIME, (1950) 170, 183–184.

Petrovic, A.M., Siebert, J.E. and Rieke, P.E., "Soil bulk density in three dimensions by computed tomographic scanning," *Soil Sci. Soc. Am. J.*, (1982) 46, 445–450.

Stern, L.A., Kirby, S.H., & Durham, W.B., "Peculiarities of methane clathrate hydrate formation and solid-state deformation, including possible superheating of water ice," *Science*, (1996) 273 (5283), pp. 1843–1848.

Tréhu, A.M., Bohrmann, G., Rack, F.R., Torres, M.E., et al., 2003. *Proc. ODP, Init. Repts.*, 204 [CDROM]. Available from: Ocean Drilling Program, Texas A&M University, College Station TX 77845-9547, USA.

Vinegar, H.J., "X-ray CT and NMR imaging of rocks," *J. Pet. Tech.*, (1986) 38, 257–259.

Wellington, S.L. and Vinegar, H.J., "X-ray computerized tomography," *J. Pet. Tech.*, (1987) 39, 885–898.

Figure Captions

Figure 1. (a) A schematic layout of the portable x-ray CT system. (b) The CT system installed in the Bridge Deck *Joides Resolution* core laboratory for ODP Leg 210.

Figure 2. An aluminum acylindrical x-ray compensator used to increase sensitivity of the x-ray CT by reducing the variation in intensity of the image striking the image intensifier. The flat regions at the edge of the compensator provide a reference area on each radiograph for normalizing for variations in x-ray intensity.

Figure 3. Radiographs taken with and without the aluminum x-ray compensator. Histograms for the mid-region of each image show how the compensator permits use of greater x-ray energy resulting in a broader distribution of pixel values. This translates into CT reconstructions with greater density resolution.

Figure 4. A single horizontal slice from a CT reconstruction of a cylindrical density reference standard.

Figure 5. Linear regression of mean attenuation values obtained using a density reference standard containing an assortment of materials. The PVC data point is not used in the regression because the high effective atomic number of the chlorine atoms increases the attenuation.

Figure 6. Radiograph of ODP Leg 204 1251B15 silty-clay sulfide-rich bioturbated core. The bright horizontal features result from disturbance of the core during recovery caused by exsolution of gas.

Figure 7. A comparison of different methods of estimating bulk density for ODP Leg 204 1251B 37. The graph shows data from x-ray radiography, Cs¹³⁷ gamma ray densiometry, gravimetric density measurements, and logging while drilling density measurements.

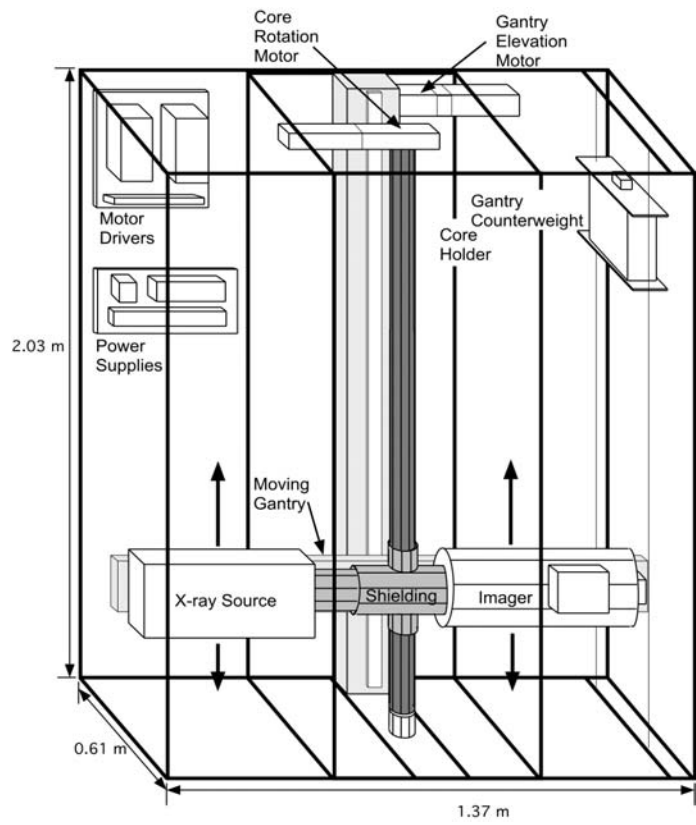
Figure 8. A simplified schematic of a hydrate dissociation experiment.

Figure 9. X-ray CT images of a synthetic hydrate dissociation experiment. The baseline image shows the location of hydrate and water ice in a sand matrix. The difference images reveal the progression of dissociation within the hydrate nodules. The gray scale bar only applies to the difference images. The rectangular highlighted regions in the difference image, acquired at 61 minutes, were used to calculate changes in hydrate density.

Figure 10. (a) The estimated change in density for water ice used as a reference material in a hydrate dissociation experiment, showing the upper and lower 95% confidence intervals as a function of region of interest size. The density changes were calculated using the difference between the baseline CT data set and a data set acquired after 44 minutes. The expected change is 0.0 g/cc. (b) Time progression for changes in density of hydrate as dissociation progresses, expressed with upper and lower 95% confidence intervals as a function of region of interest size. The final data set, taken at 44 minutes, was acquired after dissociation was determined to be complete by independent pressure measurements.

Figure 11. X-ray CT image of an interbedded sandstone from Hot Ice #1. The upper detail reveals wispy submillimeter planes of fine sand, while the lower detail shows interbedded organic laminae and small claystone clasts. The dark subhorizontal feature located approximately 10 cm below the top of the core is an ice lens.

Figure 12. X-ray CT images of core recovered at Hot Ice #1. (a) Vertical slices through an unlithified sands, with abundant fossil shells. The large bright region is a clay ironstone concrete. The rounded dense objects are quartz pebbles. (b) Horizontal images of a permafrost conglomerate cemented together by a sand/ice matrix. (c) A sandstone core with abundant mussel fossils.



(a)



(b)

Fig 1

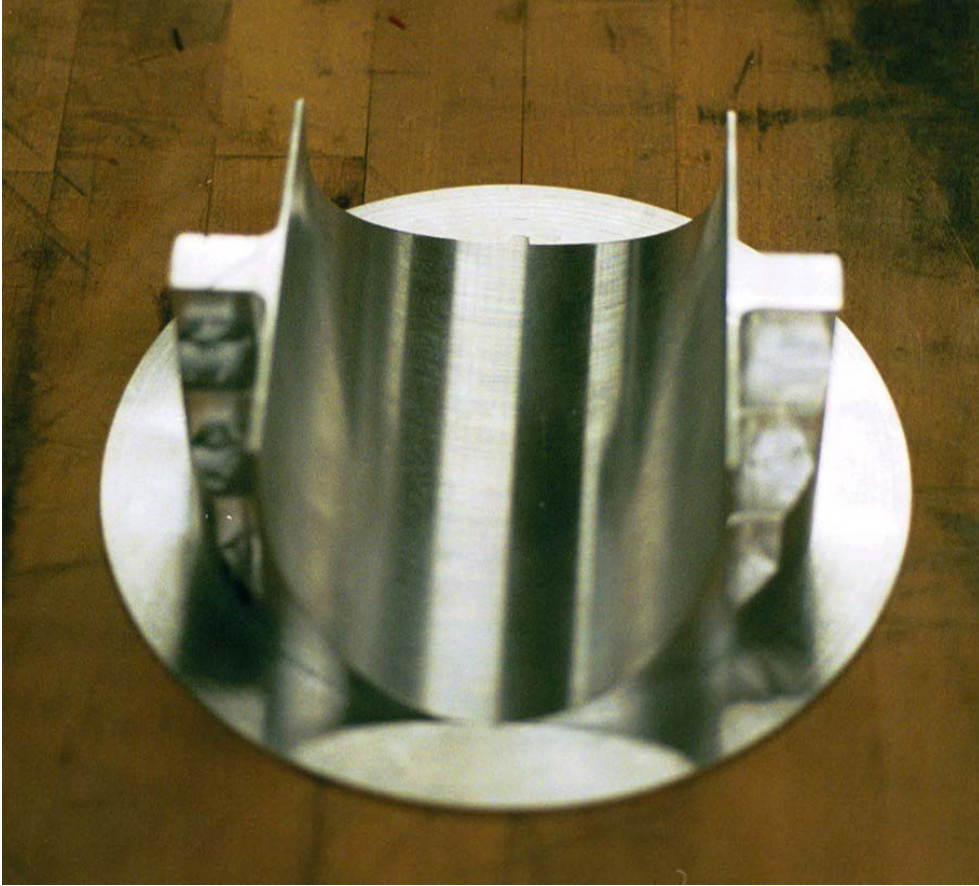
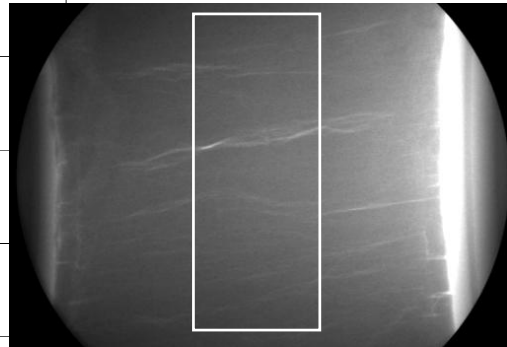
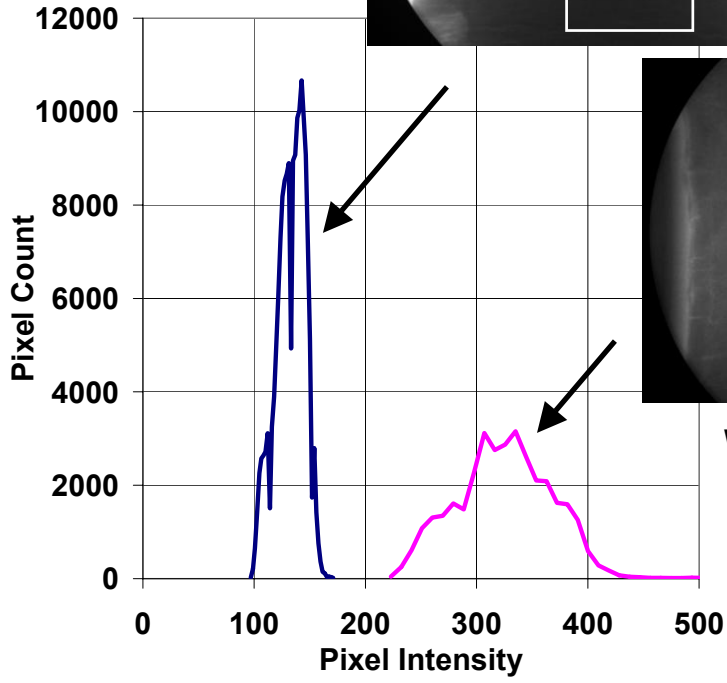
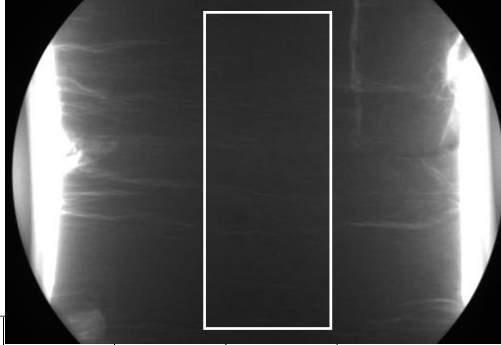


Fig 2

Without Compensator



With Compensator

Fig 3

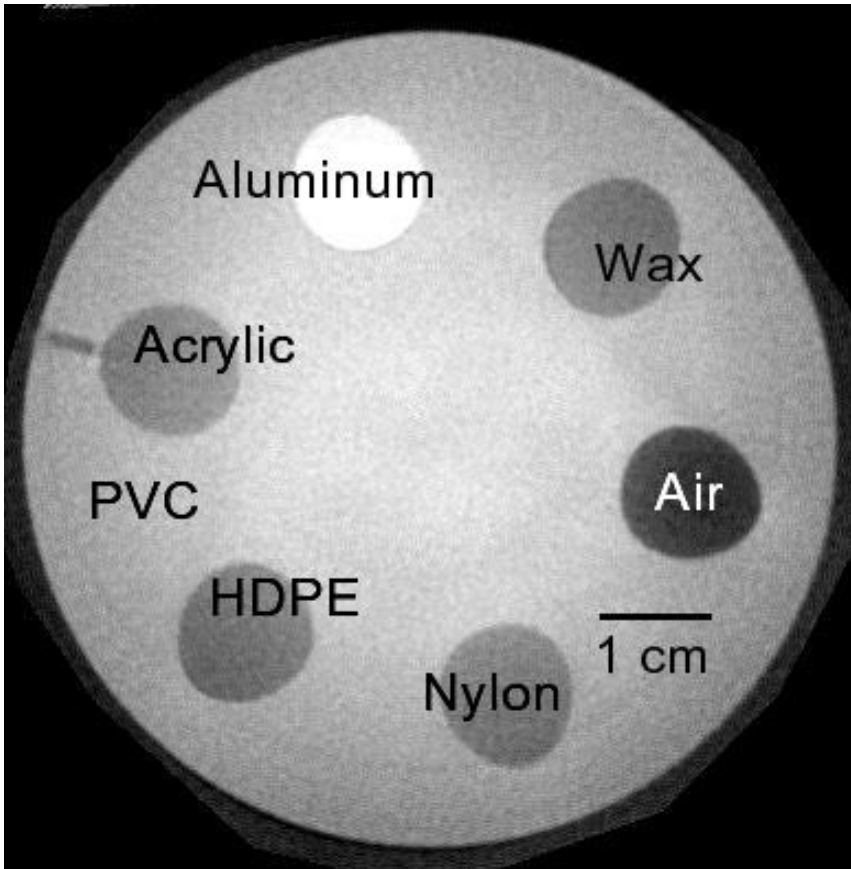


Fig 4

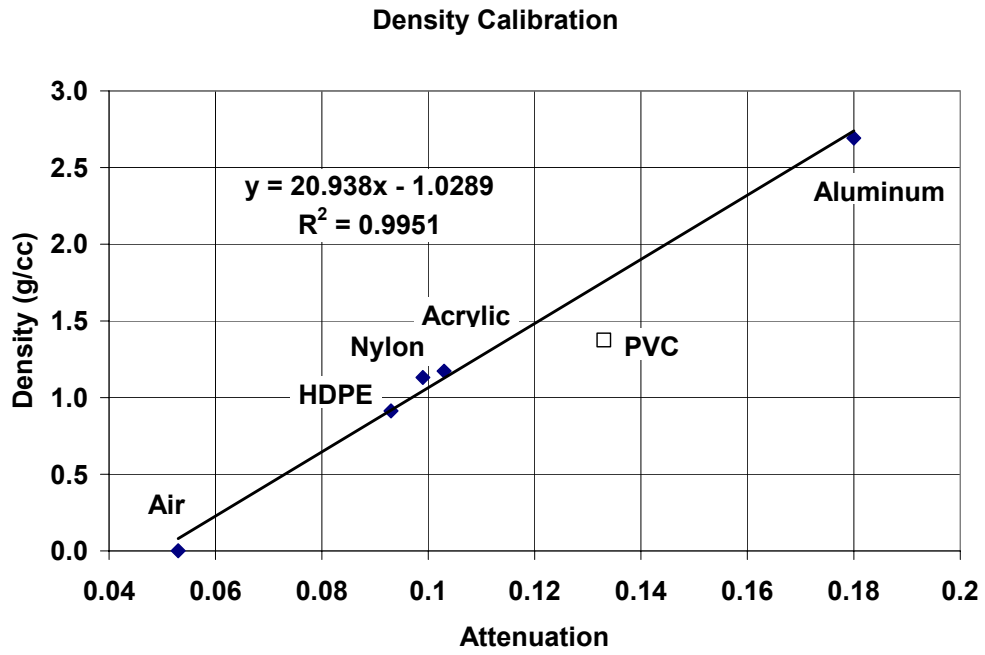


Fig 5

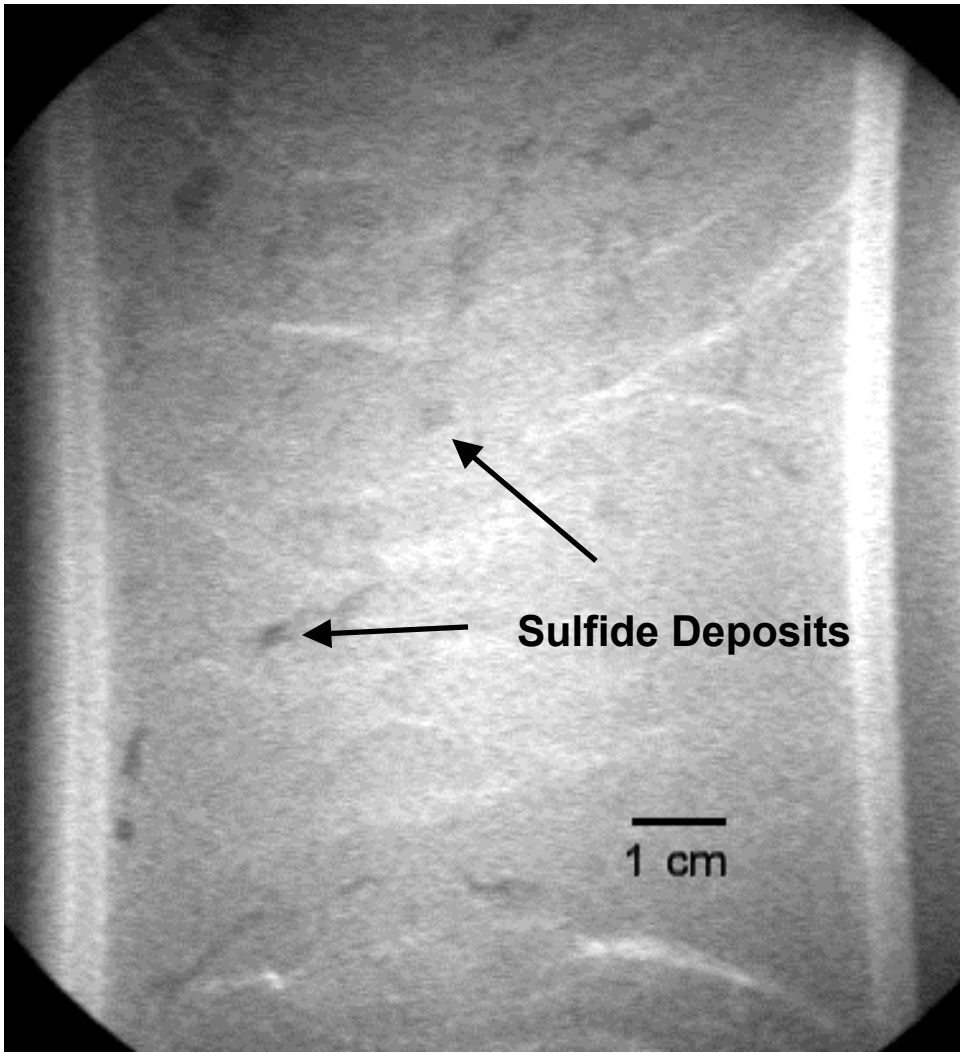


Fig 6

Leg 204 1251B 37

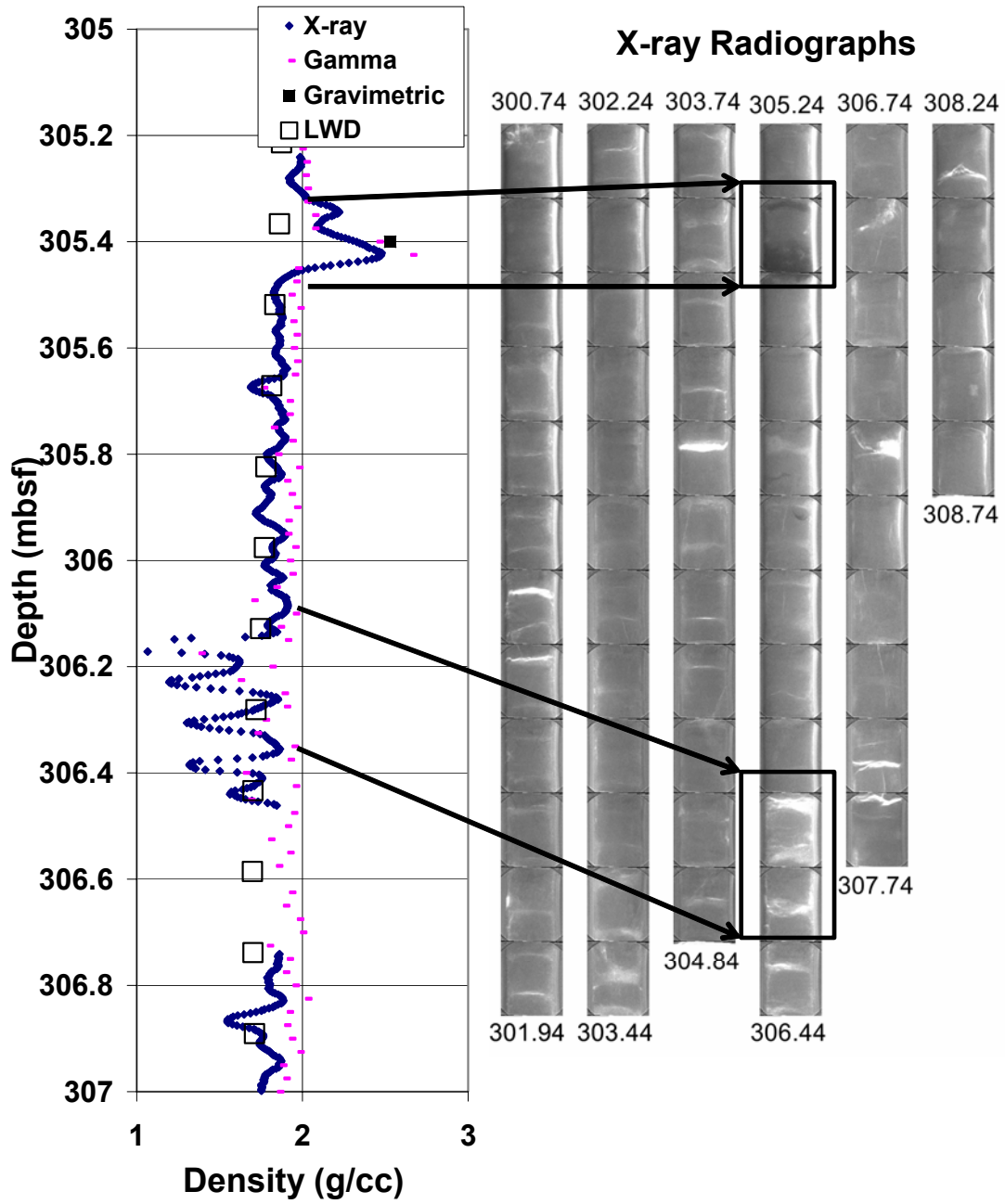


Fig 7

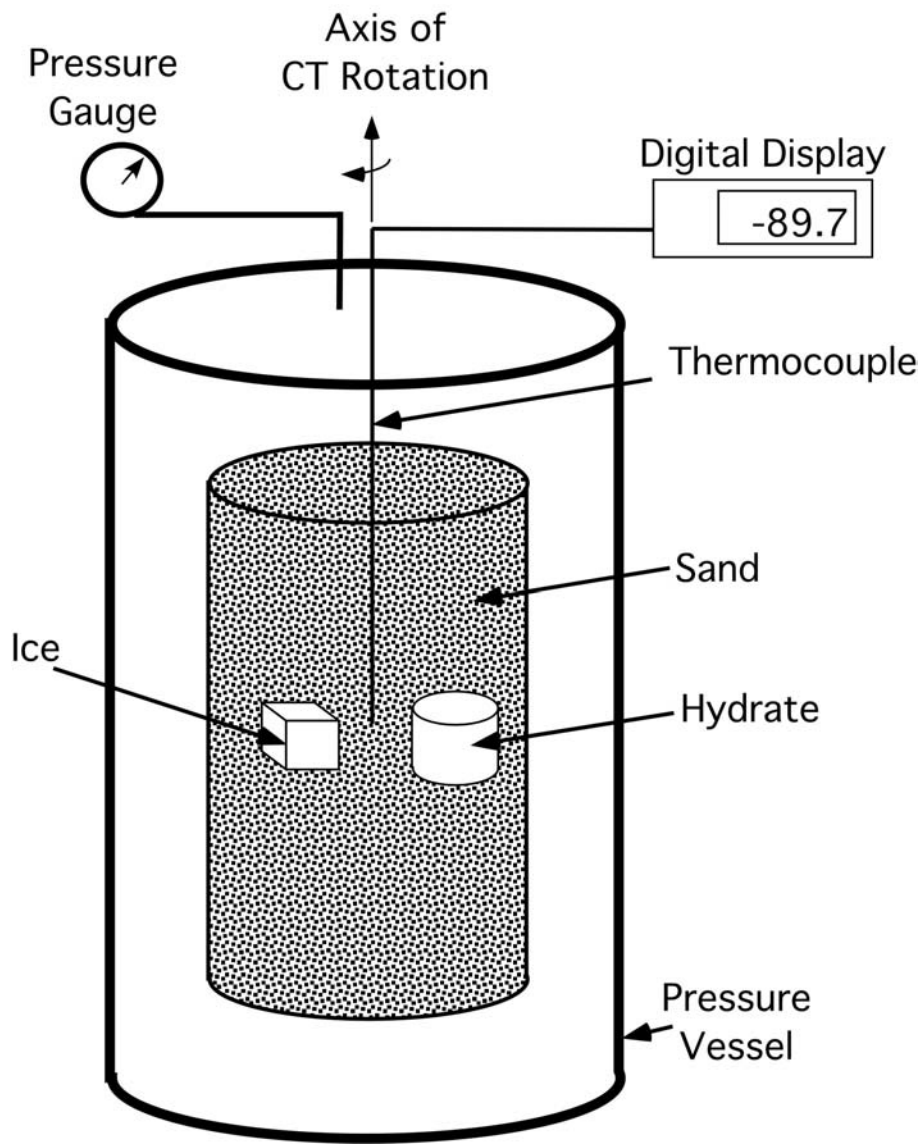


Fig 8

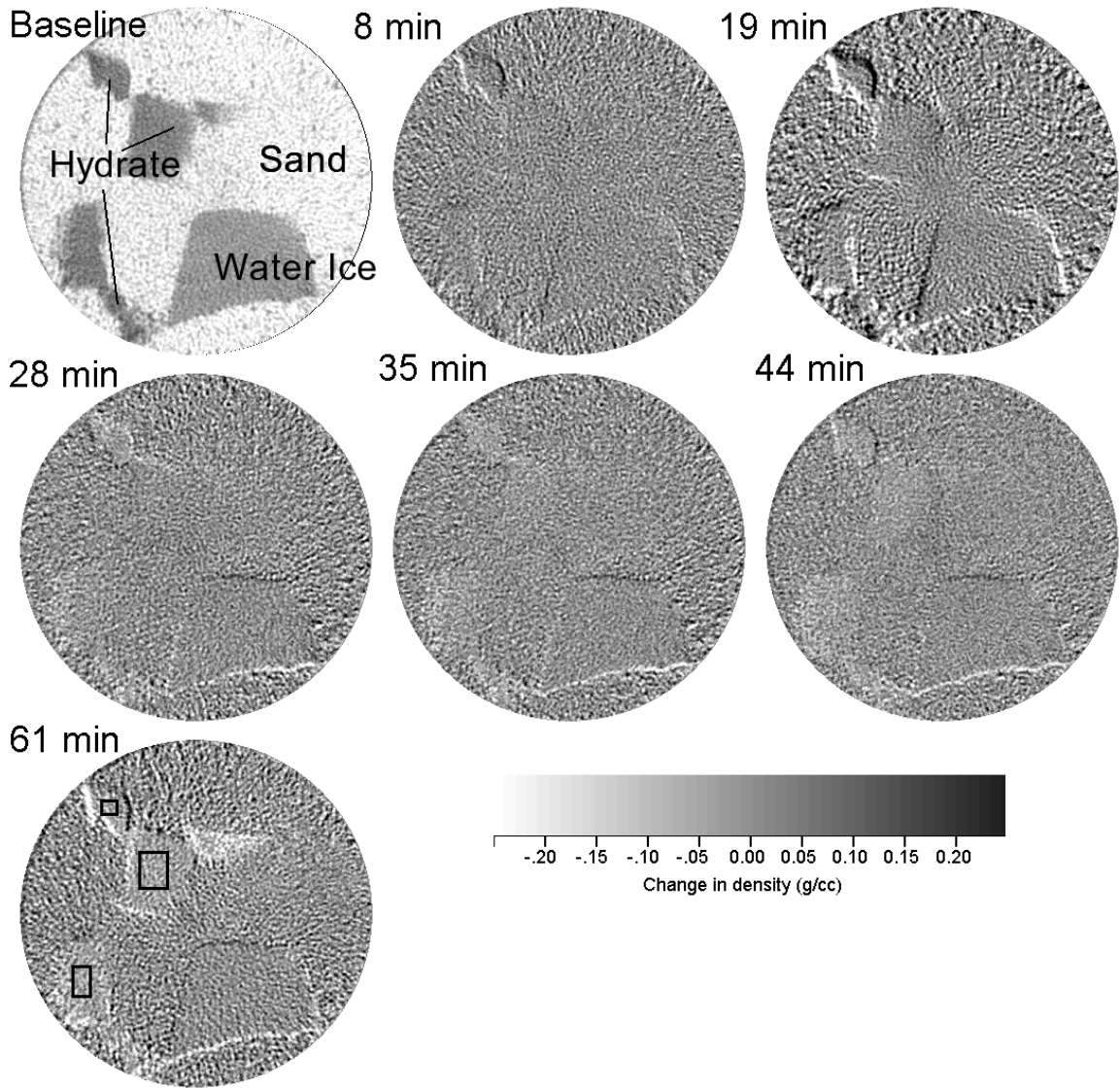


Fig 9

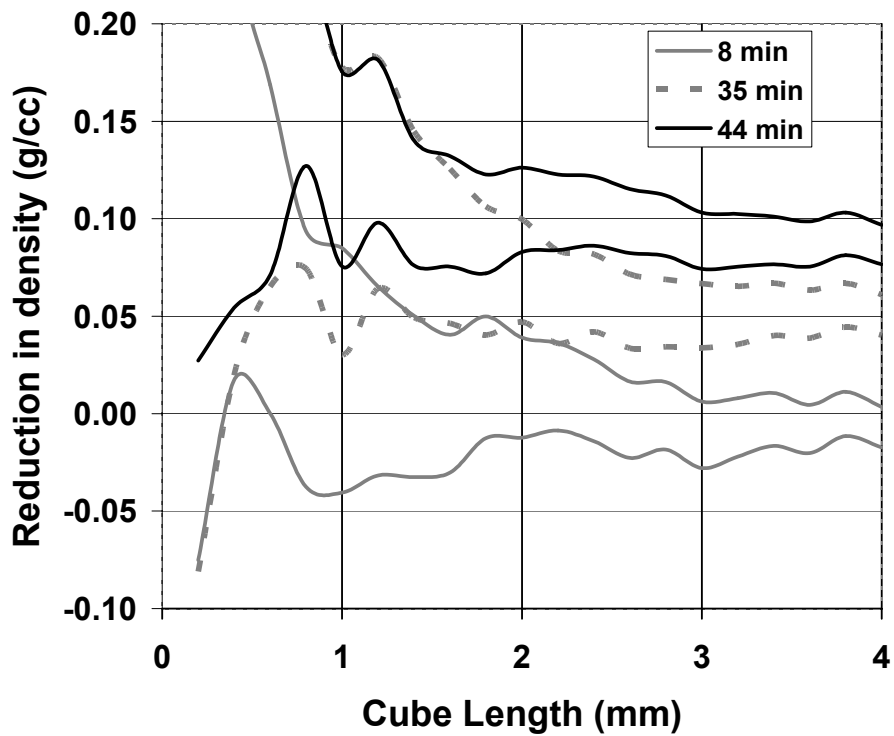
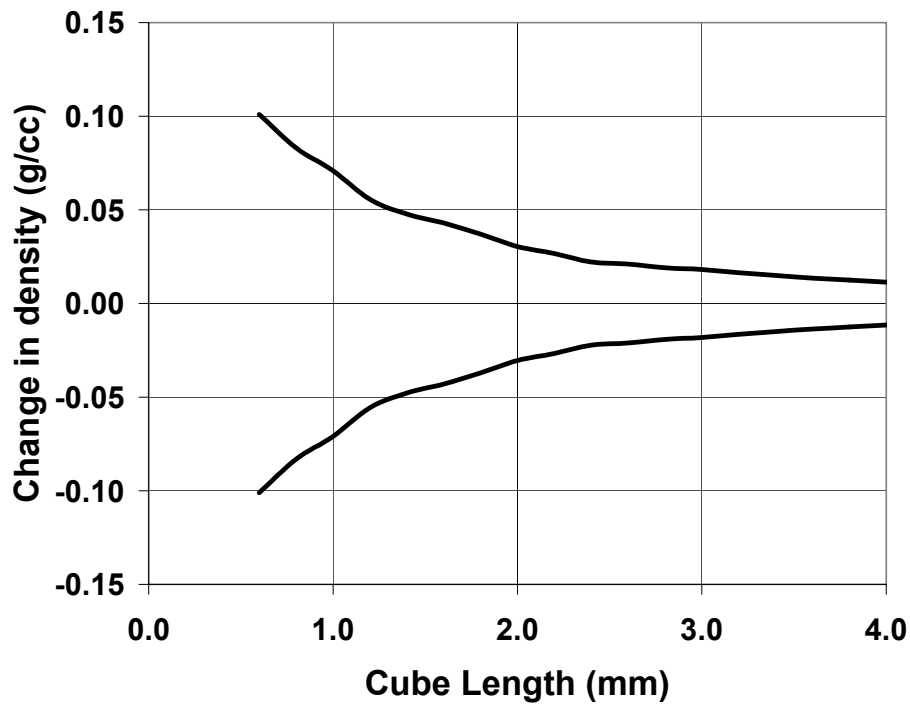


Fig
10

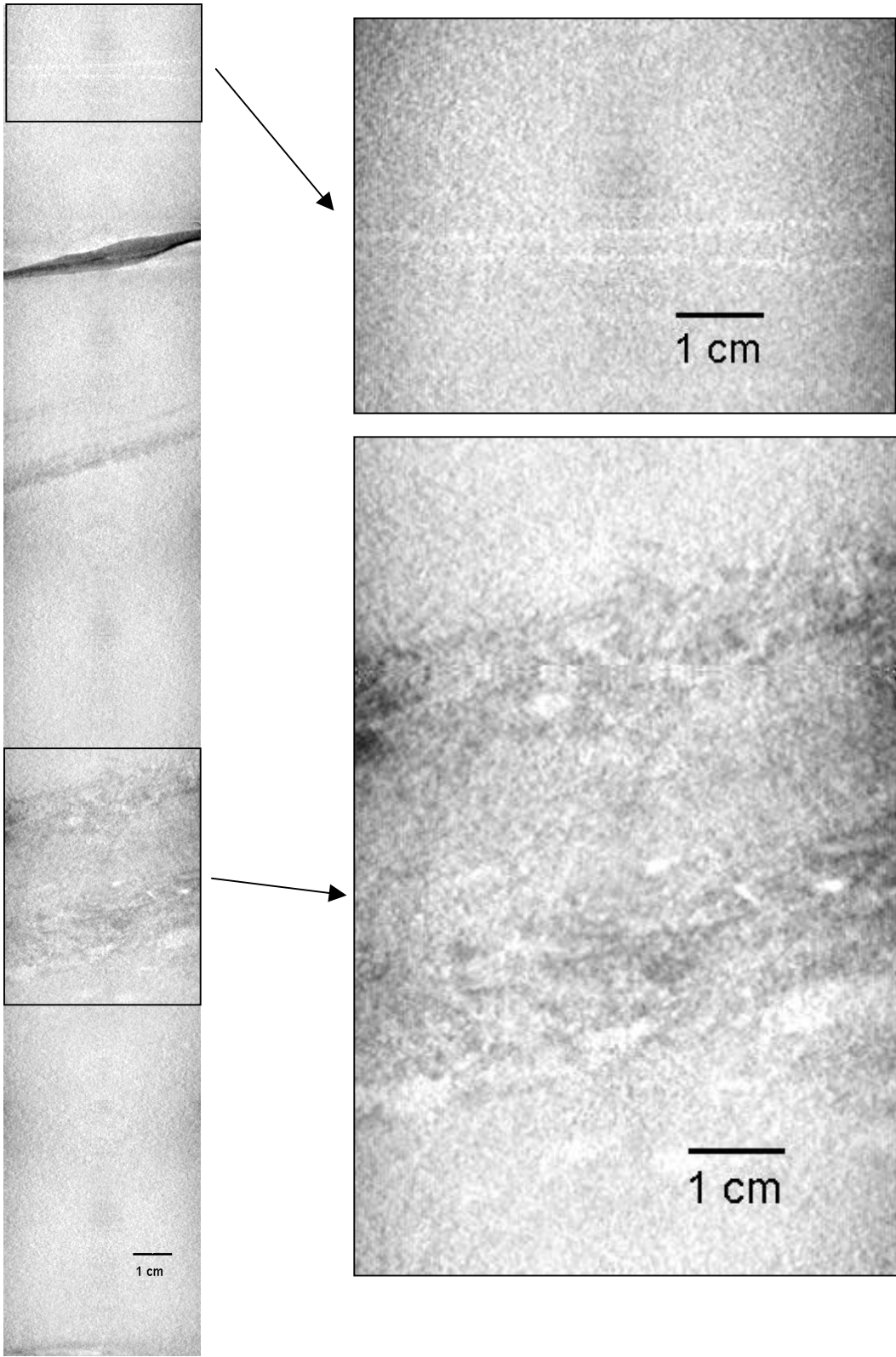
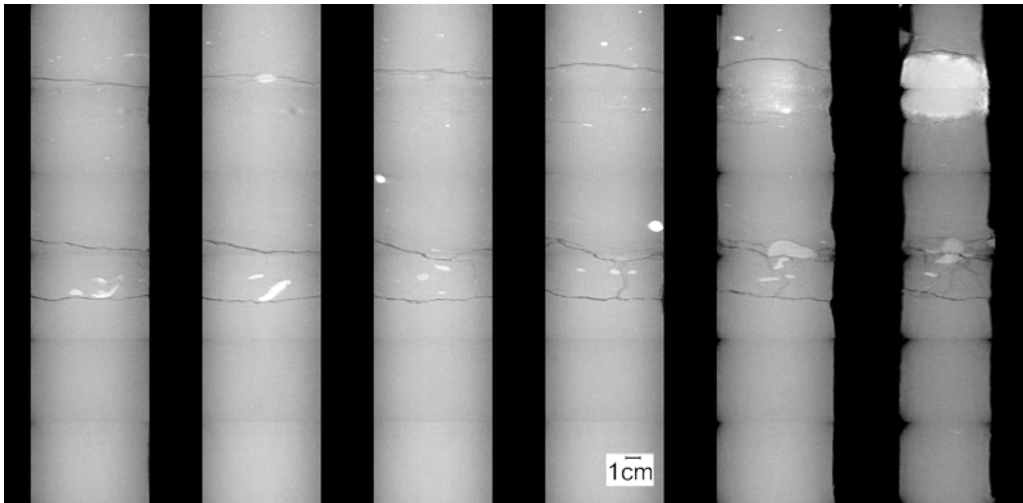
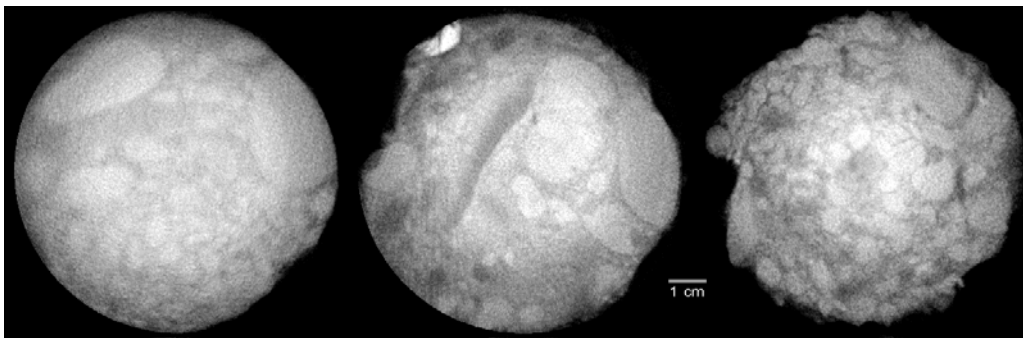


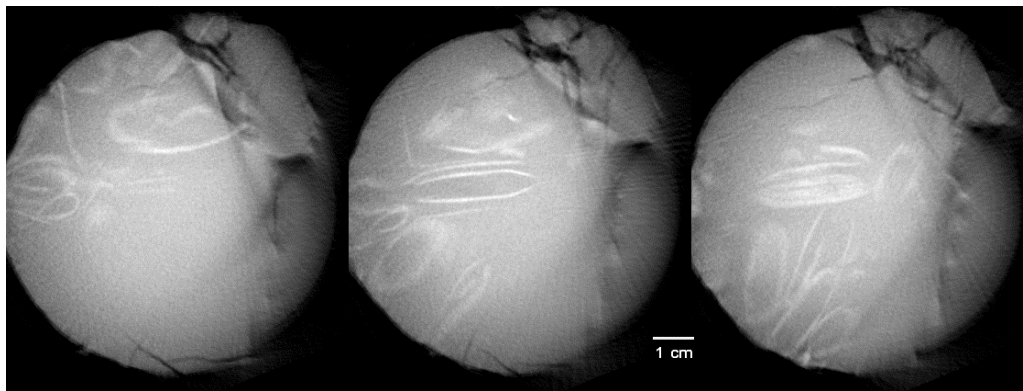
Fig 11



(a)



(b)



(c)

Fig 12